Protected Pseudohelical Edge States in $\mathbb{Z}_2$-Trivial Proximitized Graphene

Tobias Frank,* Petra Högl, Martin Gmitra, Denis Kochan, and Jaroslav Fabian
Institute for Theoretical Physics, University of Regensburg, 93040 Regensburg, Germany

(Received 7 July 2017; revised manuscript received 10 November 2017; published 9 April 2018)

We investigate topological properties of models that describe graphene on realistic substrates which induce proximity spin-orbit coupling in graphene. A $\mathbb{Z}_2$ phase diagram is calculated for the parameter space of (generally different) intrinsic spin-orbit coupling on the two graphene sublattices, in the presence of Rashba coupling. The most fascinating case is that of staggered intrinsic spin-orbit coupling which, despite being topologically trivial, $\mathbb{Z}_2 = 0$, does exhibit edge states protected by time-reversal symmetry for zigzag ribbons as wide as micrometers. We call these states pseudohelical as their helicity is locked to the sublattice. The spin character and robustness of the pseudohelical modes is best exhibited on a finite flake, which shows that the edge states have zero g factor, carry a pure spin current in the cross section of the flake, and exhibit spin-flip reflectionless tunneling at the armchair edges.

DOI: 10.1103/PhysRevLett.120.156402

Graphene is an exciting material to investigate electrical transport [1], but it also has remarkable spin properties that make it useful for spintronics applications [2,3]. One outstanding issue in graphene spintronics [4] is the enhancement of spin-orbit coupling (SOC), which is only about 10 μeV in pristine graphene [5], to realize topological effects [6] such as the quantum spin Hall state (QSHS) [7,8], anomalous quantum Hall effect [9,10], or topological superconductivity in graphene.

The most promising way to induce SOC in graphene is via proximity effects which allow graphene to inherit properties from the substrate. Substrates can break the sublattice symmetry, which has two important effects. First, an orbital gap opens due to the staggered potential, and, second, intrinsic SOC acquires a staggered term. In the original model of Kane and Mele [7], the intrinsic couplings on A and B sublattices are the same. In proximitized graphene, they can be different, such as graphene on copper [11]. The most extreme case is graphene on transition metal dichalcogenides (TMDCs), schematically depicted in Fig. 1(a). By these substrates spin-valley locking is induced in graphene, manifested in the appearance of the valley Zeeman coupling—opposite (in sign) intrinsic SOCs in the sublattices [12–14], which enables, for example, optical spin injection in graphene [15,16]. Rashba coupling is also induced which can lead to efficient charge-to-spin conversion [17]. Valley Zeeman effect can be detected as a giant spin lifetime anisotropy [18–20].

There are already experiments on graphene on TMDCs [14,21–27]. Weak localization [14,24,25,27] and spin transport measurements [21,26,28] confirm the proximity induced SOC in graphene in the range of 1 to 10 meV. Density functional theory calculations predict SOC of about 1 meV [12–14,25,29]. In the extreme case of strong SOC, as in graphene on WSe_2, inverted band structure arises [13,14,25,30], indicating the possibility of topological edge states. At the moment there is no consistent picture. The inverted structure was reported to be

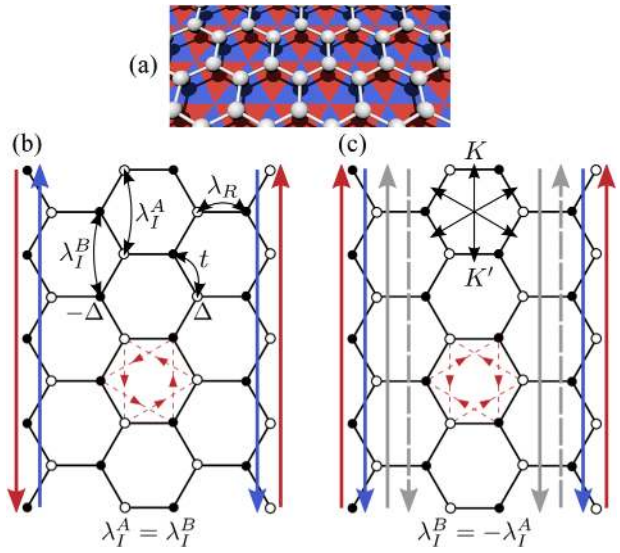

FIG. 1. Schematics of proximity induced properties in graphene. (a) Graphene placed on a symmetry-breaking substrate. (b) Hopping parameters used in our model. Sublattice A is represented as empty dots and sublattice B as filled dots. Symbols colored in red (blue) denote spin-up (spin-down) characteristics. Dashed red lines encode spin-up intrinsic SOC hoppings (signs indicated by arrows), for the uniform case of $\lambda_I^A = \lambda_I^B$, within a hexagon. Helical states and their velocity directions are indicated by long arrows. Panel (c) shows reciprocal K and K' directions with respect to the lattice. Intrinsic SOC hoppings are shown for staggered intrinsic SOC, $\lambda_I^A = -\lambda_I^B$, by red dashed lines. Solid (dashed) gray arrows indicate valley edge states located in the $\kappa = 1$ (-1) valley. Red and blue arrows show pseudohelical states carrying finite spin current along the ribbon.

topologically nontrivial ($\mathbb{Z}_2 = 1$) [14], which appears in line with the appearance of helical edge modes (termed quantum spin Hall states) [13], but is inconsistent with the statement of having a trivial system ($\mathbb{Z}_2 = 0$) [25].

We aim to provide a unified picture of the topological nature of proximity models and the existence and character of protected edge states. We introduce a modified Haldane model [31] with staggered intrinsic SOC to illustrate how edge states appear in models with spin-valley locking. There are in general two pairs of edge states formed at each edge, pseudohelical and valleylike. This makes the bulk model trivial [25], which we prove by the study of the $\mathbb{Z}_2$ phases within the intrinsic SOC space. Can protected edge states arise in a $\mathbb{Z}_2$-trivial system? Yes. And the key is to gap out the unwanted (valley) pair of states by finite-size effects. This is effortlessly realized in narrow ribbons, as we show. The remaining pair is protected against time-reversal scattering, just like the QSHS. But unlike helical states of the QSHS, our edge states are pseudohelical, being spin-up at one zigzag edge and spin-down at the other. These states are connected by reflectionless spin-flip tunneling at the armchair edges of a flake. Unlike helical, pseudohelical states carry pure spin current, and have zero g factor.

The electronic structure of a bipartite hexagonal lattice with broken sublattice and horizontal reflection symmetries, such as graphene on a substrate, can be described by the C_{3v}-symmetric Hamiltonian [13,32,33]:

$$\begin{aligned}\mathcal{H} = &-\sum_{\langle i,j\rangle,s} t c_{is}^{\dagger} c_{js} + \sum_{i,s} \xi_i \Delta c_{is}^{\dagger} c_{is} \\ &+ \frac{2i\lambda_R}{3} \sum_{\langle i,j\rangle,s,s'} [(\hat{\mathbf{s}} \times \mathbf{d}_{ij})_z]_{ss'} c_{is}^{\dagger} c_{js'} \\ &+ \frac{i}{3\sqrt{3}} \sum_{\langle\langle i,j\rangle\rangle,s,s'} \lambda_I^i \nu_{ij} [\hat{\mathbf{s}}_z]_{ss'} c_{is}^{\dagger} c_{js'}. \end{aligned} \tag{1}$$

The hopping terms are depicted in Fig. 1(b). Nearest-neighbor hopping t occurs between sites i and j, preserving spin s. The staggered potential Δ has signs $\xi_i = 1$ and -1, for sublattice A and B, respectively. Rashba SOC λ_R mixes states of opposite spins and sublattices. The unit vector $\mathbf{d}_{ij}$ points from site j to i and $\hat{\mathbf{s}}$ is the vector of spin Pauli matrices. The last term, the intrinsic SOC, is a next-nearest-neighbor hopping. It couples same spins and depends on clockwise ($\nu_{ij} = -1$) or counterclockwise ($\nu_{ij} = 1$) paths along a hexagonal ring from site j to i. This term distinguishes intrinsic SOC at different sublattices λ_I^i, where i stands for A or B. This is the principal extension of the models introduced earlier by Haldane [31], Kane and Mele [7], and McClure and Yafet [34]. The extension makes the models experimentally relevant, while introducing new physics. Following Ref. [7], we use in this work for numerical examples values of $t = 1$, $\Delta = 0.1t$, $\lambda_R = (3/2) \times 0.05t$, and $\lambda_I^A, |\lambda_I^B| = 3\sqrt{3} \times 0.06t$ if not indicated differently. In reality, we expect weaker couplings from proximity effects [13], but here our goal is to demonstrate qualitative features of the models. We will also comment on what is expected in real samples.

To illustrate the physics of our model, let us first look only at spin-up (spinless) electrons and choose the two opposite limits $\lambda_I^A = \lambda_I^B = \lambda_I$ as the *uniform* and $\lambda_I^B = -\lambda_I^A = \lambda_I$ as the *staggered* intrinsic SOC model cases. The corresponding spinless (with s_z omitted) linearized parts of Fourier transformed Hamiltonian Eq. (1) at the K/K' point are [12,33]

$$\mathcal{H}_I^{\text{uniform}} = \lambda_I \sigma_z \kappa, \tag{2}$$

$$\mathcal{H}_I^{\text{staggered}} = \lambda_I \sigma_0 \kappa. \tag{3}$$

$\kappa = \pm 1$ labels the K/K' point and σ Pauli matrices act in sublattice (pseudospin) space; see Supplemental Material [35].

The energy spectrum of a zigzag ribbon for spin-up electrons is plotted in Figs. 2(a) and 2(b). The two valleys with bulklike subbands are well visible. Between valley maxima and minima, edge modes appear due to the chiral nature of graphene [31]. Unlike edge states from uniform SOC with opposite velocities, edge states from staggered SOC have the same velocities, which produces current in the ground state, here assigned to spin-up electrons.

The spectra in Figs. 2(a) and 2(b) can be understood from simple considerations. The staggered potential $\Delta\sigma_z$ creates a gap and leads to the pseudospin-valley state $(vK, cK; vK', cK') = (B, A; B, A)$; here c and v label the conduction and valence bands. For K electrons, the phase of the Bloch wave function on sublattice A (B) rotates (increases by $2\pi/3$) counterclockwise (clockwise). For K' electrons this behavior is reversed. We now add intrinsic SOC, which can be viewed as an action of a vector potential (Peierls phase) [31], whose rotation within the sublattices is sketched in Figs. 1(b) and 1(c). If the Bloch phase rotation has the same sense as the rotation of the vector potential, the energy of the state increases. If the rotations are opposite, the energy decreases. (This is analogous to a system with an orbital momentum in a magnetic field.)

In the uniform case, the vector potential rotates counterclockwise [Fig. 1(b)] so that at K electrons in sublattice A are at higher and electrons in sublattice B are at lower energies. The opposite is true at K'. This establishes the connection to Eq. (2), which is a valley-pseudospin Zeeman coupling (with s_z omitted). Once the effective magnetic field λ_I overcomes the staggered potential Δ, the sublattice occupation becomes $(B, A; A, B)$, flipping A and B at K', and a chiral state that crosses the gap develops, as shown in Fig. 2(a). This is the well-known case of a Chern insulator [31].

In the case of staggered intrinsic SOC, the Peierls field acts on each sublattice equally in each valley [see Fig. 1(c)].

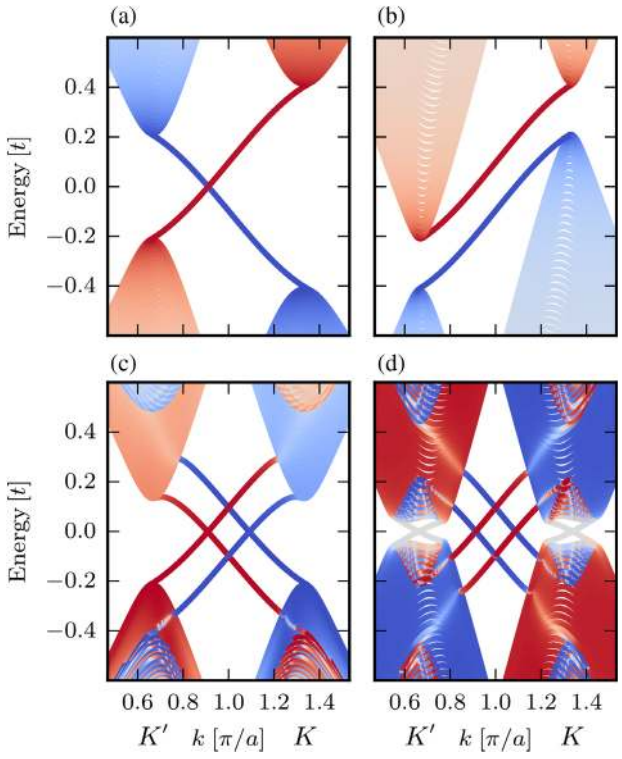

FIG. 2. Spectra of 100 unit cells wide zigzag ribbons. The color code in (a) and (b) for the spinless case denotes the sublattice expectation value: red for sublattice A and blue for sublattice B. The spectrum of the spinful case with additional Rashba SOC in (c) and (d) is color coded with the spin expectation value: red for spin-up and blue for spin-down. Left-hand column shows the uniform case, $\lambda_I^A = \lambda_I^B$, and the right-hand column shows the staggered case with strong spin-valley locking, $\lambda_I^B = -\lambda_I^A$.

The energy levels shift in opposite directions in the two valleys, and the sublattice expectation values remain $(B, A; B, A)$; see Fig. 2(b). The Hamiltonian in Eq. (3) represents a valley Zeeman coupling. If $\lambda_I \geq \Delta$, the system becomes metallic, as the conduction band in the K' point has lower energy than the valence band in the K point. Nevertheless, there are isolated propagating states, which connect states of the same sublattice expectation value from the different valleys.

Let us now reinstate both spins into the picture. The complete spectra for zigzag ribbons are obtained by mirroring the spectra in Figs. 2(a) and 2(b) around the time-reversal invariant point π/a and flipping the spin of the mirror image. If we also introduce Rashba SOC, we get additional spin mixing. The results are shown in Figs. 2(c) and 2(d). In the uniform case, the resulting band structure is additive, leading to two pairs of helical edge states, a manifestation of the QSHS [7]. The only effect of Rashba SOC is the mixing of spins in the bulk bands and a slight shift in energies.

In the staggered case, Fig. 2(d), there are also spin-polarized edge modes present, as in the QSHS. We call them pseudohelical for the reasons stated below. Contrary to the QSHS, the edge states with the same spin on different edges travel along the *same* direction, see Fig. 1(c), leading to a pure spin current (zero charge current). Rashba SOC opens a bulk gap in the valleys due to the different spin expectation values of valence and conduction bands. This gap is inverted. Inside the gap, two new edge states appear in each valley with quenched spins. Each valley contributes one mode per edge with opposite velocities on the distinct boundaries [see Fig. 1(c)]. Having both valley-centered and pseudohelical states, we term this the quantum valley spin Hall state (QVSHS) [36]. We note that similarly to the case of the QSHS [8], $\lambda_R \gg \lambda_I$ destroys the edge states.

The Hamiltonian in Eq. (1) possesses time-reversal symmetry, and has broken particle-hole and sublattice symmetries; therefore, it belongs to the class AII [37]. In two dimensions this leads to the possibility of a $\mathbb{Z}_2$ classification, which for our set of models is shown in Fig. 3, in the space of the two sublattice intrinsic SOC parameters. This map shows four distinct regions separated by gap closings, where one can expect a change in the topological invariant. $\mathbb{Z}_2$ invariants are calculated numerically [38] in Ref. [35]. The QSHS regions in the upper right and lower left corners exhibit nontrivial topologies, while the QVSHS, located on the $\lambda_I^A = -\lambda_I^B$ diagonal, is $\mathbb{Z}_2$ trivial. Bulk band structures representing this phase diagram are given in Ref. [35].

We find the staggered cases to have a trivial $\mathbb{Z}_2$ invariant, as stated in Ref. [25] for $\lambda_I^A = -\lambda_I^B$. In addition, we find that unlike zigzag ribbons, armchair ones have *no* edge states [25,35]. The valley Chern number in the staggered case is 1 (see Ref. [35]), as found also in Ref. [30]. This Chern number characterizes the states that occur inside the valley

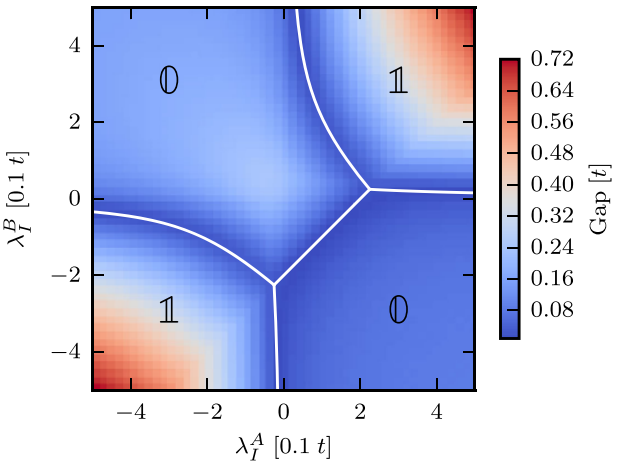

FIG. 3. $\mathbb{Z}_2$ phase space and bulk gap landscape of graphene in the $\lambda_I^A - \lambda_I^B$ plane. Color denotes the size of the gap in graphene. Solid lines are analytical expressions for a (global) bulk graphene gap closing, which separate trivial ($\mathbb{0}$) and nontrivial ($\mathbb{1}$) phases from each other. Orbital parameters and Rashba SOC are the same as in the text.

and confirms the existence of one conducting channel per edge and valley. The valley states are similar to valley states in bilayer graphene [39], where edge modes are absent in armchair ribbons as well. This absence is due to intervalley (short-range) scattering as K and K' are mapped onto each other in the armchair geometry.

Crucial for our further analysis is the localization behavior of the edge states. To get the localization length, we fit $|\psi(y)|^2 \propto \exp(-y/\lambda)$, where y is measured from the edge [35]. We find that pseudohelical edge states decay very fast, over half a unit cell ($\lambda \approx 0.4a$), whereas valley states have a much longer localization length ($\lambda \approx 9a$). This indicates that for narrow ribbons valley states should be gapped due to hybridization. A comparison of the band structures for zigzag ribbons of width of ten unit cells for uniform and staggered cases is shown in Figs. 4(a) and 4(b), respectively. Indeed, the valley states exhibit a gap in the QVSHS in Fig. 4(b), explaining the sole occurrence of apparent quantum spin Hall states in Ref. [13].

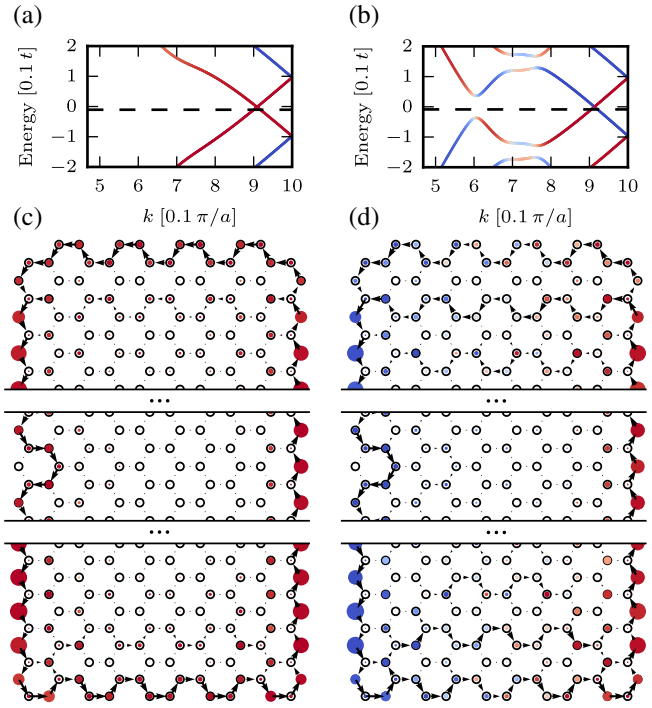

FIG. 4. Finite-sized zigzag ribbons and flakes of width of ten zigzag unit cells. Left-hand column is for the case of $\lambda_I^A = \lambda_I^B$ and right-hand column for $\lambda_I^B = -\lambda_I^A$. Panels (a) and (b) show the band structure of an infinite zigzag ribbon over half of the Brillouin zone with spin expectation values as color code (up in red, down in blue). Panels (c) and (d) show finite flakes of length of 100 zigzag cells and properties of a state that lies at energy indicated by dashed lines in (a) and (b), respectively. Empty dots denote the lattice, full dots indicate the site expectation value color coded for spin polarization, and black arrows show probability bond currents. Orbitals in the middle areas of (c) and (d) have been removed, acting as short-range scatterers. Images of flakes have been cut due to size constraints.

The larger decay length of the valley states is due to their spectral closeness to bulk states; see Fig. 2(d). We find the relation $w/a \lesssim \sqrt{3}\pi t/E_g$ between the zigzag ribbon width w and the value of the inverted gap E_g, for which valley edge states gap out due to finite-size quantization effects [35,40]. For realistic gaps [13] (in the order of meV) valley states should be gapped out in ribbons provided they are narrower than 2.5 μm, which is accessible to experiments.

With the valley states gapped out, we are left with a single pair of pseudohelical states at each edge inside the gap. What are these states and how do they compare to the helical modes of the QSHS? In particular, since the spin-up modes head in one direction along the two edges, how do the states meet in a finite flake? To clarify this question, we explored finite graphene flakes taking states from within the gap as shown in Fig. 4(a) and 4(b). To simulate short-range scattering we removed one orbital from the left zigzag edge. Additionally, we calculated spin and site expectation values as well as probability bond currents [41]. In the QSHS, Fig. 4(c), we find, as expected, a true helical edge state flowing along the boundary, avoiding the short-range scatterer and preserving its spin along z. The time-reversed partner of this state has the opposite chirality and opposite spin polarization.

The edge states appearing in the finite-size gap of the QVSHS are presented in Fig. 4(d). They have several fascinating features. (a) The probability bond current navigates around the short-range scatterer and does not scatter back. There is only the time-reversed partner, $T\psi$ of the edge state ψ, available at this energy and, as for topologically protected states, backscattering is forbidden as long as the impurity V is nonmagnetic and scattering is elastic (mathematically, $\langle\psi|V|T\psi\rangle = 0$). (b) Spin polarization is opposite on the two edges, which are formed by different sublattices. This is why we call these states *pseudohelical*—with "pseudo" describing either the pseudospin-spin locking or "not-really-helical" character of the states. Net spin current flows in this state along the zigzag direction. Also, we explicitly checked that the out-of-plane g factor of the pseudohelical states is zero, as expected since, although they are locally spin polarized, globally the pseudohelical states are spinless. (c) Further, also at odds with true helical states, which exist along the armchair edge, pseudohelical states exhibit reflectionless tunneling [35] along the armchair boundary, gradually changing their spin in Fig. 4(d) due to Rashba SOC. This tunneling connects protected modes at opposite edges by narrow channels, which could be termed wormholes, as in 3D topological insulators [42]. We discuss the transition to the bulk behavior of wider flakes in Ref. [35]. (d) We checked that the pseudohelical states are robust with respect to nonmagnetic on-site disorder up to strengths comparable to Rashba SOC [35]. Finally, our model also predicts interesting states that exist at a single edge only; see Ref. [35].

The pure spin current generated by pseudohelical states and the fact that valley states are spin unpolarized suggest that spin and charge current flows in a two-terminal geometry with $G = 4e^2/h$ for wide ribbons and fully spin-polarized current with $G = 2e^2/h$ for narrow ribbons.

To conclude, we provide a $\mathbb{Z}_2$ map for a general class of graphene Hamiltonians and show that the spin-valley locking models are $\mathbb{Z}_2$ trivial. Nevertheless, we prove that protected states exist even in such trivial systems, due to size quantization. These findings are important for graphene on substrates such as TMDCs, especially with the ability of atomically precise growth of zigzag ribbons [43].

This work was supported by the DFG SFB Grant No. 689, 1277 (A09 and B07) and GRK Grant No. 1570, and the International Doctorate Program Topological Insulators of the Elite Network of Bavaria. This project has received funding from the European Union's Horizon 2020 research and innovation programme under Grant Agreement No. 696656. The authors gratefully acknowledge the Gauss Centre for Supercomputing e.V. for funding this project by providing computing time on the GCS Supercomputer SuperMUC at Leibniz Supercomputing Centre (LRZ).

*tobias.frank@physik.uni-regensburg.de

[1] A. H. Castro Neto, F. Guinea, N. M. R. Peres, K. S. Novoselov, and A. K. Geim, Rev. Mod. Phys. **81**, 109 (2009).
[2] I. Žutić, J. Fabian, and S. Das Sarma, Rev. Mod. Phys. **76**, 323 (2004).
[3] J. Fabian, Acta Phys. Slovaca **57**, 565 (2007).
[4] W. Han, R. K. Kawakami, M. Gmitra, and J. Fabian, Nat. Nanotechnol. **9**, 794 (2014).
[5] M. Gmitra, S. Konschuh, C. Ertler, C. Ambrosch-Draxl, and J. Fabian, Phys. Rev. B **80**, 235431 (2009).
[6] Y. Ren, Z. Qiao, and Q. Niu, Rep. Prog. Phys. **79**, 066501 (2016).
[7] C. L. Kane and E. J. Mele, Phys. Rev. Lett. **95**, 226801 (2005).
[8] C. L. Kane and E. J. Mele, Phys. Rev. Lett. **95**, 146802 (2005).
[9] Z. Qiao, S. A. Yang, W. Feng, W.-K. Tse, J. Ding, Y. Yao, J. Wang, and Q. Niu, Phys. Rev. B **82**, 161414(R) (2010).
[10] Y. Yang, Z. Xu, L. Sheng, B. Wang, D. Y. Xing, and D. N. Sheng, Phys. Rev. Lett. **107**, 066602 (2011).
[11] T. Frank, M. Gmitra, and J. Fabian, Phys. Rev. B **93**, 155142 (2016).
[12] M. Gmitra and J. Fabian, Phys. Rev. B **92**, 155403 (2015).
[13] M. Gmitra, D. Kochan, P. Högl, and J. Fabian, Phys. Rev. B **93**, 155104 (2016).
[14] Z. Wang, D.-K. Ki, H. Chen, H. Berger, A. H. MacDonald, and A. F. Morpurgo, Nat. Commun. **6**, 8339 (2015).
[15] Y. K. Luo, J. Xu, T. Zhu, G. Wu, E. J. McCormick, W. Zhan, M. R. Neupane, and R. K. Kawakami, Nano Lett. **17**, 3877 (2017).
[16] A. Avsar, D. Unuchek, J. Liu, O. L. Sanchez, K. Watanabe, T. Taniguchi, B. Özyilmaz, and A. Kis, ACS Nano **11**, 11678 (2017).
[17] M. Offidani, M. Milletarì, R. Raimondi, and A. Ferreira, Phys. Rev. Lett. **119**, 196801 (2017).
[18] A. L. Benítez, J. F. Sierra, W. S. Torres, A. Arrighi, F. Bonell, M. V. Costache, and S. O. Valenzuela, Nat. Phys. **14**, 303 (2018).
[19] A. W. Cummings, J. H. Garcia, J. Fabian, and S. Roche, Phys. Rev. Lett. **119**, 206601 (2017).
[20] T. S. Ghiasi, J. Ingla-Ayns, A. A. Kaverzin, and B. J. van Wees, Nano Lett. **17**, 7528 (2017).
[21] A. Avsar, J. Y. Tan, T. Taychatanapat, J. Balakrishnan, G. K. W. Koon, Y. Yeo, J. Lahiri, A. Carvalho, A. S. Rodin, E. C. T. O'Farrell, G. Eda, A. H. Castro Neto, and B. Özyilmaz, Nat. Commun. **5**, 4875 (2014).
[22] C. P. Lu, G. Li, K. Watanabe, T. Taniguchi, and E. Y. Andrei, Phys. Rev. Lett. **113**, 156804 (2014).
[23] S. Larentis, J. R. Tolsma, B. Fallahazad, D. C. Dillen, K. Kim, A. H. MacDonald, and E. Tutuc, Nano Lett. **14**, 2039 (2014).
[24] Z. Wang, D.-K. Ki, J. Y. Khoo, D. Mauro, H. Berger, L. S. Levitov, and A. F. Morpurgo, Phys. Rev. X **6**, 041020 (2016).
[25] B. Yang, M.-F. Tu, J. Kim, Y. Wu, H. Wang, J. Alicea, R. Wu, M. Bockrath, and J. Shi, 2D Mater. **3**, 031012 (2016).
[26] S. Omar and B. J. van Wees, Phys. Rev. B **95**, 081404(R) (2017).
[27] T. Völkl, T. Rockinger, M. Drienovsky, K. Watanabe, T. Taniguchi, D. Weiss, and J. Eroms, Phys. Rev. B **96**, 125405 (2017).
[28] A. Dankert and S. P. Dash, Nat. Commun. **8**, 16093 (2017).
[29] T. P. Kaloni, L. Kou, T. Frauenheim, and U. Schwingenschlögl, Appl. Phys. Lett. **105**, 233112 (2014).
[30] A. M. Alsharari, M. M. Asmar, and S. E. Ulloa, Phys. Rev. B **94**, 241106(R) (2016).
[31] F. D. M. Haldane, Phys. Rev. Lett. **61**, 2015 (1988).
[32] M. Gmitra, D. Kochan, and J. Fabian, Phys. Rev. Lett. **110**, 246602 (2013).
[33] D. Kochan, S. Irmer, and J. Fabian, Phys. Rev. B **95**, 165415 (2017).
[34] J. W. McClure and Y. Yafet, *Proceedings of the Fifth Conference on Carbon* (Pergamon Press, New York, 1962), Vol. 1, p. 22.
[35] See Supplemental Material at http://link.aps.org/supplemental/10.1103/PhysRevLett.120.156402 for the linearized Hamiltonian, numerical $\mathbb{Z}_2$ calculations, band structure topologies, and valley Chern numbers. Ribbon properties, like armchair band structures and zigzag state localization, are discussed. An absence condition for valley states is derived and the pseudohelical state emergence is shown. We present single-edge localized states as well as the on-site disorder dependence of helical and pseudohelical states.
[36] A similar abbreviation was introduced in a graphene system with magnetic impurities. S. F. Islam and C. Benjamin, Carbon **110**, 304 (2016).

[37] S. Ryu, A. P. Schnyder, A. Furusaki, and A. W. W. Ludwig, New J. Phys. **12**, 065010 (2010).
[38] D. Gresch, G. Autès, O. V. Yazyev, M. Troyer, D. Vanderbilt, B. A. Bernevig, and A. A. Soluyanov, Phys. Rev. B **95**, 075146 (2017).
[39] Z. Qiao, W. K. Tse, H. Jiang, Y. Yao, and Q. Niu, Phys. Rev. Lett. **107**, 256801 (2011).
[40] Y. M. Lin, V. Perebeinos, Z. Chen, and P. Avouris, Phys. Rev. B **78**, 161409(R) (2008).
[41] T. B. Boykin, M. Luisier, and G. Klimeck, Eur. J. Phys. **31**, 1077 (2010).
[42] G. Rosenberg, H.-M. Guo, and M. Franz, Phys. Rev. B **82**, 041104 (2010).
[43] P. Ruffieux, S. Wang, B. Yang, C. Sánchez-Sánchez, J. Liu, T. Dienel, L. Talirz, P. Shinde, C. A. Pignedoli, D. Passerone, T. Dumslaff, X. Feng, K. Müllen, and R. Fasel, Nature (London) **531**, 489 (2016).